Neurosci. Bull. June, 2023, 39(6):929–946
https://doi.org/10.1007/s12264-022-00995-7

www.neurosci.cn
www.springer.com/12264

ORIGINAL ARTICLE

REEP1 Preserves Motor Function in SOD1^{G93A} Mice by Improving Mitochondrial Function via Interaction with NDUFA4

Siyue Qin[1] · Pan You[1] · Hui Yu[1] · Bo Su[1]

Received: 11 May 2022 / Accepted: 25 September 2022 / Published online: 15 December 2022

Abstract A decline in the activities of oxidative phosphorylation (OXPHOS) complexes has been consistently reported in amyotrophic lateral sclerosis (ALS) patients and animal models of ALS, although the underlying molecular mechanisms are still elusive. Here, we report that receptor expression enhancing protein 1 (REEP1) acts as an important regulator of complex IV assembly, which is pivotal to preserving motor neurons in SOD1^{G93A} mice. We found the expression of REEP1 was greatly reduced in transgenic SOD1^{G93A} mice with ALS. Moreover, forced expression of REEP1 in the spinal cord extended the lifespan, decelerated symptom progression, and improved the motor performance of SOD1^{G93A} mice. The neuromuscular synaptic loss, gliosis, and even motor neuron loss in SOD1^{G93A} mice were alleviated by increased REEP1 through augmentation of mitochondrial function. Mechanistically, REEP1 associates with NDUFA4, and plays an important role in preserving the integrity of mitochondrial complex IV. Our findings offer insights into the pathogenic mechanism of REEP1 deficiency in neurodegenerative diseases and suggest a new therapeutic target for ALS.

Keywords REEP1 · Amyotrophic lateral sclerosis · Mitochondria · Complex IV assembly · NDUFA4

Supplementary Information The online version contains supplementary material available at https://doi.org/10.1007/s12264-022-00995-7.

✉ Bo Su
bxs103@sdu.edu.cn

[1] Department of Cell Biology, Shandong Provincial Key Laboratory of Mental Disorders, School of Basic Medical Sciences, Shandong University, Jinan 250012, China

Introduction

Amyotrophic lateral sclerosis (ALS) is one of the most common motor neuron diseases characterized by progressive degeneration of motor neurons (MNs) in the brainstem and spinal cord. Many ALS cases, referred to as sporadic ALS, are not genetically transmitted and their causes remain enigmatic. Only 5%–10% of ALS cases are familial, most of which are associated with repeat expansions of the *C9ORF72* gene or mutations in genes encoding copper-zinc superoxide dismutase (SOD1), TAR DNA binding protein 43 (TDP-43), or fused in sarcoma (FUS) [1]. The cellular and molecular mechanisms underlying MN loss in both familial and sporadic ALS are still unknown, and effective treatments are extremely limited.

Many ALS-associated genes, including *SOD1*, *TDP-43*, *FUS*, and *C9ORF72*, play roles in mitochondrial functions. Evidence gathered from *in vitro* or *in vivo* disease models and ALS patients, strongly implicates the dysfunction of mitochondria as a core component of ALS. Reductions in cellular respiration and ATP production are well documented in ALS and animal models of ALS. In the postmortem spinal cord of sporadic ALS patients, the activity of complexes I, II, III, and IV (CI, CII, CIII, and CIV) is reduced [2, 3]. Consistent with this, decreased CI + III, CII + III, and CIV activities also occur in the spinal cord of SOD1^{G93A} transgenic mice (G93A mice) [4]. However, the mechanism underlying the impairments of mitochondrial respiration in ALS remains largely unknown.

Receptor expression enhancing proteins (REEPs), a family of six proteins (REEP1–6), were first identified by their ability to enhance the cell surface expression of olfactory receptors and other G protein-coupled receptors [5, 6]. Later studies revealed that REEPs are localized on the tubular endoplasmic reticulum (ER) membrane to coordinate

ER shaping and microtubule dynamics [7]. Among these REEPs, REEP1 is under intensive investigation because of its close association with hereditary spastic paraplegia (HSP), a rare neurodegenerative disorder characterized by progressive degeneration of corticospinal motor neurons [8]. Given the truncating nature of most genetic mutations of REEP1, it has been suggested that REEP1 mutations cause disease by a loss-of-function mechanism [9, 10]. In addition, REEP1-knockout mice display a gait disorder and axonal degeneration closely resembling those seen in HSP patients [11, 12]. At the molecular level, REEP1 has been reported to control the structural and dynamic changes of intracellular membrane structures, including the ER, trafficking vesicles, and lipid droplets, through a microtubule-associated pathway [11–15]. Also, it has been shown that REEP1 is localized in mitochondria [8], however, its function in mitochondria remains unknown.

In the present study, we investigated the expression of REEPs in the spinal cord of the widely-used ALS mouse model G93A mice. We found that the reduction of REEP1 expression is a distinguishing feature of patients and the mouse model of ALS. Overexpression of REEP1 by an AAV-mediated approach prevents motor neuron neurodegeneration in G93A mice by improving mitochondrial function. Our study connects reduced expression of REEP1 to impaired oxidative phosphorylation (OXPHOS) activity in ALS.

Materials and Methods

Animals

Mouse surgery and procedures were approved and conducted in accordance with the Institutional Animal Care and Use Committee of Shandong University. Transgenic SOD1 G93A mice on the C57BL/6 background (B6.Cg-Tg(SOD1*G93A)1Gur/J, Stock No: 004435) were from the Jackson Laboratory, Bar Harbor, USA.

Lumbar Spinal Cord Injection of AAV

Adeno-associated virus serotype 1 encoding GFP (AAV1-GFP) or human REEP1 with Flag tag (AAV1-hREEP1-Flag) under the neuron-specific promoter eSYN, were purchased from WZ Bioscience, Jinan, China. AAVs were injected as previously described [16]. After anesthesia by isoflurane/oxygen inhalation, the mouse vertebral column was immobilized on a stereotactic frame to expose the lumbar spine. Bupivacaine/lidocaine (1:1 v/v) was injected around a small skin incision in the back of an anesthetized mouse. The L1 vertebra was exposed by removing the small spinal muscles and ligaments attached to its dorsal surface. Then the dorsal portion of the vertebra was removed to expose the spinal cord. 3 μL AAV (10^{13} viral particles per mL) was injected into two locations at a depth of 1 mm rostral to the transection through a glass micropipette attached to a Hamilton syringe (Hamilton, Reno, USA). The micropipette was left in place for 5 min before the withdrawal. The skin was sutured, and the mice were placed on a temperature-controlled warm pad for a few hours before being returned to their home cage.

Grip Strength and Footprint Test

A grip strength meter (Bioseb, Pinellas Park, USA) was used to measure hind limb grip strength. Both hind paws were placed on a bar connected to the meter. As a mouse grasped the bar, the pull force in grams was recorded on a digital force transducer. After 5 trials, the single best-recorded value was used for statistical analysis. The grip strength meter was periodically calibrated by the manufacturer. Footprints were analyzed using a customized runway (50 cm long, 5 cm wide, and both sides bordered by walls). The fore and hind paws were first dipped into the purple or orange paint. Each mouse was placed on a runway covered by aluminum foil where they ran toward an enclosed dark box. Stride length was presented as the mean distance of forward movement between each stride. The resulting data were further plotted in GraphPad Prism 8 software (GraphPad Software Inc., San Diego, USA).

Electrophysiological Recordings of Skeletal Muscles

We made electromyographic recordings of the compound muscle action potential (CMAP) evoked in hind limb muscles by supramaximal stimulation of the sciatic nerve using the PowerLab 4/35 data acquisition system, a FE155 Stimulator HC, a FE136 Animal Bio Amp, and needle electrodes from ADInstruments (Colorado Springs, USA) as well as ring surface electrodes from Natus Neurology (Orlando, USA). Mice were anesthetized by isoflurane/oxygen inhalation and immobilized with a piece of tape. Reference and ground needle electrodes were inserted into the sacrum and tail tip. The fur around the hind limb was removed and ring-positive and negative electrodes were placed on the gastrocnemius muscle with contact gel. The stimulating needle electrode was inserted into the muscle near the sciatic nerve. A 1–10 mV stimulus 0.1 ms in duration was applied at a frequency of 10 Hz. The recording data were exported to Excel and maximal CMAP was plotted with GraphPad Prism 8 software.

Cell Culture and Transfection

All the cell culture reagents were from ThermoFisher Scientific (Auburn, USA). Lenti-X 293T cells from Takara Bio (Shiga, Japan) were grown and transfected in Dulbecco' modified Eagle's medium (Sigma Aldrich, St. Louis, USA), supplemented with 10% fetal bovine serum (FBS) (v/v) and 1% penicillin-streptomycin in a 5% CO_2 humid incubator at 37°C. Lenti-X 293T cells were tested and confirmed to be free of mycoplasma contamination. The Lenti-X 293T cells were transfected with TransIT®-293 Transfection Reagent according to the manufacturer's protocol. 24 h before the experiments, 500 ng DNA/well was used to transiently transfect 1×10^5 cells in a 24-well plate. The Lenti-X 293T cell line was used for up to 20 passages. The International Cell Line Authentication Committee does not list the cells used in this study as commonly misidentified cell lines. No authentication was conducted during the experiments.

Plasmids

The original plasmid backbone pcDNA3.1 (+) was from Invitrogen (Waltham, USA). To generate Strep or Strep-Flag tagged plasmids, coding sequences of Strep-tag and Flag tag were synthesized and cloned into pcDNA3.1(+) by Gibson assembly (NEB, Ipswich, USA). All the plasmids used in this study are listed in Table S2.

Generation of REEP1-KO and Rescued Cell Lines

REEP1-KO cells were generated from Lenti-X 293T cells with a CRISPR/Cas9 system designed in our lab. pSpCas9(BB)-2A-Puro (PX459) V2.0 was a gift from Zhang Feng (Addgene, Watertown, USA) [17]. The single guide (sg) RNA targeting sequence was predicted using the online CRISPR design tool (https://benchling.com). Lenti-X 293T cells were first transfected with the PX459-gREEP1 vector, which targeted 5′-TCACAGACATCTTCC TTTGT-3′ of the *REEP1* gene. After puromycin selection, the cells were diluted and seeded in 96-well plates at 1 cell/well to isolate monoclonal cells without REEP1 expression as determined by western blot analysis. To generate rescue cell lines, REEP1-KO cells were transfected with the pcDNA3.1(+)-Zeo-Strep vector, pcDNA3.1(+)-REEP1-Strep, and pcDNA3.1(+)-REEP1Δ101-110-Strep. Of note, the sequence targeted by sgRNA in wild-type (WT) and mutant REEP1 plasmids was codon optimized to 5′-TTT ACCGACATATTCCTTTGT-3′ to resist CRISPR/Cas9 cleavage. After zeocin selection, monoclonal cells were obtained by the method described above.

Cell Proliferation

The proliferation of REEP1-KO and control cells was evaluated by growth curve assays. 10^5 cells were seeded in each well of a 6-well plate. 12 h after seeding, the cells were harvested and the time point was set as Time 0. Then cells were harvested at the indicated time. After staining with DAPI, images were captured by Celldiscoverer 7 (Zeiss, Oberkochen, Germany), and cell numbers were counted.

Immunocytochemistry and Immunofluorescence

Immunohistochemistry was applied using the peroxidase anti-peroxidase protocol. Paraffin-embedded spinal cord sections were first deparaffinized in xylene, rehydrated in graded ethanols, and incubated in Tris-buffered saline (TBS, 50 mmol/L Tris-HCl, and 150 mmol/L NaCl, pH 7.6) for 10 min before antigen retrieval in 1× immunoDNA retriever with citrate (BSB 0021, Bio SB, Santa Barbara, USA). The sections were rinsed with distilled H_2O, incubated in TBS for 10 min, and blocked with 10% normal goat serum (NGS) in TBS for 30 min at room temperature. The sections were further incubated with primary antibodies in TBS containing 1% NGS overnight at 4°C and immunostained by the peroxidase-anti-peroxidase-based method as we described previously [18].

For immunofluorescence staining, cells cultured on coverslips were washed three times with pre-warmed PBS buffer and fixed with 4% paraformaldehyde for 15 min at room temperature. After washing the coverslips 3 times with PBS, the cells were permeabilized by 0.5% Triton X-100 for 25 min. For tissues, deparaffinization and antigen retrieval processing were as above. Then the cell and tissue samples were blocked with 10% NGS (Sigma Aldrich) in PBS for 30 min at room temperature followed by incubation with primary antibodies in PBS containing 1% NGS at 4°C overnight. The antibodies were washed out with PBS, and cells were incubated with 10% NGS in PBS for 10 min and then with Alexa Fluor-conjugated secondary antibodies (Life Technologies, Carlsbad, USA) (1:250) for 2 h at room temperature protected from light. After that, cells were rinsed three times with PBS and the nuclei were stained with DAPI. Finally, they were again washed three times with PBS and mounted with Fluoromount-G mounting medium (Southern Biotech, Birmingham, USA). The antibodies used in this study are listed in Table S3.

Fluorescence Microscopy

Fluorescent images were captured with a Zeiss automated microscope, Celldiscoverer 7, and Zeiss LSM800 (all microscopes controlled by Zen software, Zeiss). For live-cell time-lapse imaging, Lenti-X 293T cells were seeded in a 24-well plate. 24 h after seeding, the culture plate was placed into the Celldiscoverer 7 system with a stage-top incubator (37°C, 5% CO_2).

Immunoblot Analysis and Blue Native PAGE

For immunoblots, cells or tissues were lysed in cell lysis buffer (Cell Signaling Technology, Danvers, USA), containing 1 mmol/L phenylmethanesulfonyl fluoride (PMSF; Millipore, Burlington, USA), protease inhibitor cocktail (Sigma Aldrich), and phosphatase inhibitor cocktail (Sigma Aldrich). The lysate was centrifuged at 14,000 g for 15 min at 4°C. The protein concentration of the supernatant was measured by BCA assay (ThermoFisher Scientific). Equal amounts of proteins (20 μg) were separated by 10% SDS-PAGE and transferred to a polyvinylidene fluoride (PVDF) membrane (Millipore). The membranes were blocked with 10% non-fat dry milk in TBST and incubated with primary antibodies at 4°C overnight. After rinsing 3 times in TBST, peroxidase-conjugated secondary antibodies were applied for 1 h at room temperature, and the blots were developed with Immobilon Western Chemiluminescent HRP Substrate (Millipore). Images were captured using the ChemiDoc Touch Imager (Bio-Rad, CA, USA). The primary antibodies used in this study are listed in Table S3. The blue-native page was applied according to the user's guide of the Novex® native gel electrophoresis system (Life Technologies). Taken briefly, mitochondrial OXPHOS complexes were extracted in 1× NuPage buffer with digitonin (8 g/g mitochondria ratio). After incubation for 30 min on ice, the lysate was centrifuged at 14,000 g for 15 min at 4°C to remove insoluble debris. The protein concentration was determined, and 50 μg of protein combined with 0.25% G-250 was loaded onto a 4–12% precast Bis-Tris gradient gel (Invitrogen, Carlsbad, USA). After electrophoresis, the complexes were electroblotted onto PVDF membranes and incubated with human Mitococktail antibodies against CI–CV subunits.

Immunoprecipitation

Cells were collected 24 h after transfection and lysed with lysis buffer (100 mmol/L Tris-HCl, 150 mmol/L NaCl, 1 mmol/L EDTA, and 1% NP40, pH 8.0) containing 1 mmol/L PMSF (Millipore), protease inhibitor cocktail (Sigma Aldrich), and phosphatase inhibitor cocktail (Sigma Aldrich). The lysate was centrifuged at 14,000 g for 15 min at 4°C. The supernatant was incubated with MagStrep "type3" XT beads (IBA Lifesciences, Göttingen, Germany) overnight at 4°C. The beads were washed three times with lysis buffer and eluted with BXT buffer (IBA Lifesciences). The eluted proteins were subjected to western blot or mass spectrometric analysis.

Subcellular Fractionation

Cells were homogenized in IB-1 solution (in mmol/L: 225 mannitol, 75 sucrose, 0.1 EGTA, 20 HEPES; pH 7.4). The total homogenate was centrifuged twice at 600 g for 5 min at 4°C. Subsequently, the supernatant was collected and centrifuged at 7,000 g for 10 min at 4°C to obtain an enriched mitochondrial fraction. This fraction was washed in IB-2 solution (in mmol/L: 225 mannitol, 75 sucrose, 20 HEPES; pH 7.4) followed by centrifugation at 9,000g for 10 min. The pellets were suspended in MRB buffer (in mmol/L: 250 mannitol, 0.5 EGTA, 5 HEPES; pH 7.4) to obtain a crude mitochondrial fraction. This fraction was further overlaid on top of 8 mL Percoll medium (225 mmol/L mannitol, 25 mmol/L HEPES, 1 mmol/L EGTA, and 30% Percoll (v/v); pH 7.4) and centrifuged at 95,000 g for 30 min at 4°C in an SW40 Ti rotor. The pellet was suspended in MRB buffer again, followed by centrifugation at 6,300 g for 10 min at 4°C to obtain purified mitochondria. To obtain the ER fraction, the supernatant was centrifuged at 20,000g for 30 min at 4°C. The pellet consisted of a lysosomal fraction also containing plasma-membrane contamination. Further centrifugation of the supernatant (100,000g for 1 h at 4°C) resulted in the isolation of ER (pellet) and a cytosolic fraction (supernatant).

For sub-mitochondrial compartment fractionation, isolated pure mitochondria were suspended in an isolation medium (in mmol/L: 225 mannitol, 75 sucrose, 0.1 EGTA, 20 HEPES; pH 7.4) with digitonin at 0.12 mg digitonin/mg mitochondria and stirred gently on ice for 15 min. Then the digitonin-treated samples were diluted with 3 volumes of isolation medium and centrifuged at 9,000 g for 10 min to get supernatant A. The pellet re-suspended in isolation buffer was sonicated for 30 s on ice and centrifuged at 6,500 g for 10 min followed by centrifugation at 144,000 g for 60 min at 4°C to sediment the inner membrane vesicles. The supernatant was collected as a matrix fraction. Supernatant A was centrifuged at 144,000 g for 60 min at 4°C to sediment outer membrane vesicles as pellets and the supernatant was collected as the inner membrane space fraction.

TMRM Staining

Lenti-X 293T or REEP1-KO cells were grown in 24-well plates at 70% confluence at the time of data collection. Cells were incubated with TMRM (200 nM, ThermoFisher Scientific) in fresh culture medium for 30 min in a CO_2 incubator. After two washes with 100 μL PBS containing 0.2% BSA, the plates were read by Celldiscoverer 7 with the RFP/TRITC filter set at Ex/Em = 548/575 nm. Data were analyzed with Zen software.

ATP Measurement

ATP levels were assessed by an ATP Colorimetric/Fluorometric Assay Kit (Biovision, Waltham, USA). Cells (1×10^6) were lysed in 100 μL ATP assay buffer on ice. the cell lysate was deproteinized using a 10-kDa spin column. 20 μL of the sample was added to a 96-well plate and the volume was adjusted

to 50 µL/well with ATP Assay Buffer. Enough reagent to generate a reaction mix (ATP assay buffer: ATP probe: ATP converter: Developer, at 11:1:1:1) was mixed for all samples and standards. 50 µL of the reaction mixture was added to each well of the 96-well plate, mixed well, and incubated at room temperature for 30 min, protected from light. The absorbance at 570 nm was measured with a microplate reader (Bio-Rad). To generate a standard curve, 0, 2, 4, 6, 8, and 10 µL ATP standard (1 mmol/L) were added to a series of wells and the volume was adjusted to 50 µL/well with ATP Assay Buffer to generate 0, 2, 4, 6, 8, and 10 nmol/well of ATP Standard. The curve was calculated following the manufacturer's instructions.

Analysis of Mitochondrial Complex IV Activity

Mitochondrial complex IV (cytochrome c oxidase) activity was measured using a cytochrome oxidase activity colorimetric assay kit (Biovision) following the manufacturer's instructions. Briefly, 5 µg of isolated mitochondria in cytochrome oxidase assay buffer was added to each well of a 96-well plate. For negative control, an equal volume of Enzyme Dilution Buffer was added. Then 120 µL of the diluted cytochrome c was added to each sample and the control. The spectrophotometer was set at 550 nm on the kinetic program for 30 min at 30-s intervals. The decrease in optical density (OD) over 30 min was recorded. The rate of the reaction was calculated by changes in OD: ΔOD/min by using the maximum linear rate. The oxidation of cytochrome c by complex IV is a biphasic reaction with an initial fast burst followed by a slower activity.

Quantitative Mass Spectrometry

To identify the specific binding partners of REEP1, we used a proteomic approach according to a previously published protocol [19]. Briefly, the control vector and REEP1-Strep were transfected into Lenti-X 293T cells with TransIT®-293 transfection reagent (Mirus, Houston, USA). After immunoprecipitation with MagStrep "type3" XT beads, proteins were eluted with BXT buffer (IBA Lifesciences) and separated by 4%–12% Mini-PROTEAN®TGX™ precast protein gels (Bio-Rad). After running for 10 min, 1 cm of the gel was cut and subjected to in-gel trypsin digestion. Tryptic peptides were labeled with ^{16}O or ^{18}O and then mixed for differential isotopic analysis. Labeled peptides were analyzed by LC-MS/MS using an UltiMate 3000 LC system (Dionex, Sunnyvale, USA) interfaced with a Velos Pro Ion Trap/Orbitrap Elite hybrid mass spectrometer (ThermoFisher Scientific). Peptides were identified by comparing the resultant MS/MS spectra against the Swiss-Prot database using Mascot database search software (version 2.4, Matrix Science, Chicago, USA). Strict trypsin specificity was applied with one missed cleavage allowed. The $^{18}O/^{16}O$ ratio of each peptide was calculated using Proteomics Tools software (available at https://github.com/shengqh/RCPA.Tools).

RNA Extraction and Reverse Transcription-Quantitative PCR (RT-qPCR)

Total RNA was extracted from Lenti-X 293T cells using the RNAeasy mini kit (Qiagen, Germantown, USA) according to the manufacturer's protocols. cDNA was synthesized by using High-Capacity cDNA Reverse Transcription Kits (ThermoFisher Scientific) with random primers. Quantitative reverse-transcription PCR (qPCR) was performed using the SYBR Premix Ex Taq kit (Takara Bio) in a CFX96 real-time PCR system (Bio-Rad) following the manufacturer's protocol. The thermocycling conditions were as follows: 95°C for 30 s, followed by 40 cycles of 95°C for 5 s and 60°C for 30 s. The mRNA levels of the targeted protein were normalized to GAPDH using the 2-ΔΔCq method. The primers used for RT-qPCR are listed in Table S2.

Differentiation of SH-SY5Y Cells

SH-SY5Y cells (ATCC, CRL-2266) were differentiated using a combination of previously reported protocols [20, 21]. Briefly, undifferentiated SH-SY5Y cells were maintained in a growth medium composed of Opti-MEM (#31985070, Gibco, Waltham, USA) supplemented with 5% FBS and 1% penicillin/streptomycin. To induce differentiation, cells were first seeded on an uncoated plate and, on the following day, the medium was changed to a differentiation medium composed of Opti-MEM, 1% FBS, 1% penicillin/streptomycin, and 10 µmol/L all-trans retinoic acids (R2625, Sigma Aldrich). After 3 days of differentiation, the medium was changed to fresh differentiation medium again and cultured for another 3 days. The cells were then split and seeded on poly-*D*-lysine-treated plates or coverslips. On the following days, the medium was changed to neuronal growth medium composed of Neurobasal medium (# A3582901, Gibco) supplemented with brain-derived neurotrophic factor (50 ng/mL) (#248-BD, Novus Bio/R&D Systems, Minneapolis, USA), KCl (20 mmol/L) (#P5405, Sigma), 2% B27 (#17564-044, Gibco), 1% Glutamax, 1% penicillin/streptomycin, and 10 µmol/L retinoic acids for an additional three days. Then the medium was exchanged again with fresh neuronal growth medium. After 18 days of differentiation, neuronal cells were fixed for immunofluorescence staining or lysed in cell lysis buffer for immunoblot analysis. For neuronal viability assays, differentiated neurons plated in 96-well plates were exposed to 100 µmol/L H_2O_2 or 10 µmol/L Tunicamycin for 24 h. Cell viability was measured using Cell Counting Kit-8 (Dojindo Molecular Technologies, Rockville, USA) following the manufacturer's instructions.

Sholl Analysis

Using images with a single microglial cell or astrocyte in the frame, we applied Sholl analysis using ImageJ (NIH, Bethesda, USA) after adjusting the image threshold accordingly. We used the segmented line tool to determine both the center of the soma and the length of the longest integrated radius. Data were grouped with their respective categories [non-transgenic littermates (NTG), G93A/GFP, G93A/REEP1] At least 5 cells were analyzed per animal with at least 3 animals examined per genotype. The average number of intersections of glial cells from NTG, G93A/GFP, and G93A/REEP1 mice at each radius was plotted.

Image Analysis

Images were analyzed with Zen software or Imaris (Bitplane, Belfast, UK). The acquired images were processed by deconvolution (regularized inverse filter) by ZEN software. All confocal images of mitochondria and neuromuscular junctions (NMJs) were reconstructed using the "easy 3D" module in Imaris. At least 200 NMJs from each mouse were counted. The ER structure was extracted using the SURFACE tools in Imaris following the manufacturer's instructions. Mitochondrial and ER lengths were calculated from single-plane images using Image-Pro Plus software. The length was defined as the Feret maximum. All immunoblot images were analyzed using ImageJ.

Statistical Analysis

Student's *t*-test, one-way analysis of variance (ANOVA) followed by Tukey's multiple comparisons test, and two-way ANOVA followed by Bonferroni multiple comparisons test were applied using GraphPad Prism 8 software (GraphPad Software Inc.). Detailed information about the statistical analysis for each experiment is presented in the figure legends. Data are the mean ± SEM. P <0.05 was considered to be statistically significant.

Results

Reduced Expression of REEP1 in ALS Patients and G93A Mice

As increasing evidence suggests that REEPs are involved in neurodegenerative diseases like HSP [22], we explored the relationship between REEPs and the classical motor neuron disease, ALS. Making use of an already published transcriptome dataset of the lumbar spinal cord from sporadic ALS patients and age-matched controls [23], we showed that REEP1 and REEP2, but not other REEPs were greatly reduced in these patients (Fig. S1A and B). Consistent with the findings in sporadic ALS cases, transcriptome analysis of motor neurons (MNs) derived from iPSCs (induced pluripotent stem cells) from familial ALS patients harboring a SOD1 A4V mutation demonstrated that REEP1 expression was significantly lower in SOD1A4V MNs than in their isogenic controls (Fig. S1C). Since the widely-used G93A mice develop phenotypes closely mimicking familial and sporadic ALS patients, we next studied the expression of REEPs in the spinal cord of G93A mice and their NTGs. Compared with NTG mice, the expression of REEP1 in the spinal cord was reduced significantly in 120-day-old G93A mice (Fig. 1A and B). In addition, we evaluated the REEP1 expression in G93A mice before and after the onset of the locomotor phenotype. There was likely a time-dependent reduction of REEP1 in G93A mice. At 30 days old, G93A mice showed a trend of decrease in REEP1 expression. The expression of REEP1 decreased by 40% in 60-day-old G93A mice compared with NTG mice. At 90 days old, a further decrease of 30% in REEP1 expression was noted in G93A mice (Fig. S1D). The above results suggest that the reduction of REEP1 expression is a distinguishing feature of patients and a mouse model of ALS.

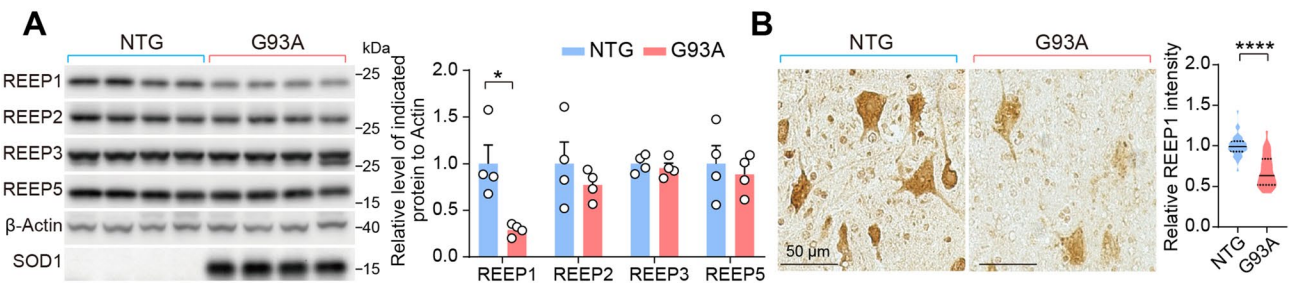

Fig. 1 Reduction of REEP1 in the spinal cord of G93A mice. **A** Representative immunoblots and quantification of REEP expression in the spinal cord of NTG (non-transgenic) and G93A mice (n = 4 mice per group). **B** Representative immunohistochemical staining of REEP1 in the lumbar spinal cord of NTG (n = 30 neurons from 3 mice) and G93A mice (n = 35 neurons from 3 mice). Scale bars, 50 μm. Data are the mean ± SEM. *P <0.05, ****P <0.0001, two-tailed Student's *t*-test.

Forced Expression of REEP1 Abolishes Skeletal Muscle Atrophy in G93A Mice

We then examined the impact of REEP1 upregulation in spinal motor neurons on behavioral deficits and survival in G93A mice. Since G93A mice have an onset of symptoms at ~60 days and the survival endpoint at ~150 days, we bilaterally injected adeno-associated virus serotype 1 encoding human REEP1 under the neuron-specific promoter eSYN (AAV1-hREEP1-Flag) into the lumbar spinal cord of 45-day-old G93A mice. The motor performance of G93A mice was evaluated by tail suspension, grip strength, and footprint tests after the age of 70 days (Fig. 2A). We first examined the expression of REEP1 in the spinal cord. To explore the cellular distribution of exogenously-expressed REEP1, spinal cord tissue from G93A mice injected with AAV1-hREEP1-Flag (G93A/REEP1) was stained with anti-Flag and anti-NeuN (neuronal nuclear protein) antibodies. As expected, REEP1-Flag was predominantly expressed in NeuN-positive cells, suggesting that REEP1 was successfully expressed in neuronal cells (Fig. S2A). In addition, immunoblot analysis of subcellular fractions further demonstrated that exogenously-expressed REEP1 was present in both ER and mitochondrial fractions, which displayed the same distribution pattern as endogenous REEP1 (Fig. S2B and C). We then compared the expression of REEP1 in AAV-injected G93A mice; immunoblot analysis revealed that G93A/REEP1 mice had a twofold increase of total REEP1 in the lumbar cord of G93A mice compared to GFP-injected G93A mice (G93A/GFP) (Fig. 2B). Surprisingly, the overall life-span of G93A/REEP1 mice was extended when compared with G93A/GFP mice (Fig. 2C), and the motor deficits of G93A mice were remarkably attenuated by REEP1 upregulation (Fig. 2D–F). While G93A/GFP mice showed hind limb folding into the abdomen with an infrequent clasping of their hind limbs, G93A/REEP1 mice exhibited greatly improved performance in tail suspension tests (Fig. 2D, S2D and Video S1). In addition, the declining muscle strength and gait abnormalities in G93A/GFP mice were also alleviated in G93A/REEP1 mice (Figs 2D, E, S2E, and Video S2).

Loss of NMJ integrity due to motor neuron denervation is a prominent feature of G93A mice [24]. Denervation occurs before the symptomatic stage and translates into reduced electrical potential in affected muscles [25]. We then applied electrophysiological tests to measure the CMAP, which is the sum of action potentials in the muscle in response to non-invasive spinal cord electrical stimulation. Decreasing CMAP values in G93A mice reflected NMJ denervation, which was partially restored by REEP1 upregulation (Fig. 2F). Consistent with the improved motor performance, G93A/REEP1 mice displayed well-preserved hindlimb skeletal muscles and alleviated NMJ denervation compared with G93A/GFP mice (Fig. 2G, H). Moreover, we also determined the expression of Agrin, Wnt3, and muscle-specific kinase (MuSK) in muscle tissue from NTG, G93A/GFP, and G93A/REEP1 mice. These three proteins are key regulators of NMJs, in which Agrin and Wnt3 are secreted by motor neurons while MuSK is mainly expressed in skeletal muscle [26]. As expected, G93A/REEP1 mice exhibited stronger expression of Agrin and Musk in skeletal muscles than in G93A/GFP mice (Fig. 2I). There was also a trend of increased levels of Wnt3 in G93A/REEP1 skeletal muscles (Fig. 2I). Therefore, these data strongly support the conclusion that augments expression of REEP1 in neurons in the spinal cord is sufficient to preserve motor function in G93A mice.

Protection Against MN Loss and Gliosis in G93A Mice via REEP1 Upregulation

Since MN numbers significantly decrease in the ventral horn of endpoint G93A mice [27], we next determined the effects of REEP1 overexpression on MN survival in G93A mice. By either Nissl or Choline Acetyltransferase (Chat) staining, we found that the MN numbers in the ventral horn of G93A/REEP1 mice significantly increased when compared to G93A/GFP mice (Fig. 3A, B). Neuroinflammation is a prominent pathological feature of ALS, characterized by the proliferation and activation of microglia and astrocytes, as extensively reported in G93A mice [27]. To assess the extent of gliosis, we immunostained activated microglia and astrocytes in the spinal cord of NTG, G93A/GFP, and G93A/REEP1 mice with specific antibodies against ionizing Ca^{2+}-binding adaptor molecule 1 (Iba1) and glial fibrillary acidic protein (GFAP) respectively. Quantification revealed remarkably reduced microgliosis and astrogliosis in the spinal cord of G93A/REEP1 mice (Fig. 3C, D). In addition to the reduced number of microglial cells, we also observed that microglia cells seemed to be more ramified in the spinal cord of G93A/REEP1 mice than G93A/GFP microglial cells. Thus, we then applied Sholl analysis, which is widely used to quantify the complexity of dendritic arbors. The data confirmed that microglial cells display greatly reduced complexity in G93A/GFP mice, and this was partially restored in G93A/REEP1 mice (Fig. S3A). Similarly, astrocytes in G93A/REEP1 mice also demonstrated more ramifications than in G93A/GFP mice (Fig. S3B). Thus, these data support the conclusion that restoring the expression of REEP1 protects against MN loss and gliosis in G93A mice.

Loss of REEP1 Impairs Mitochondrial Function

As REEP1 is closely associated with the ER and mitochondrial function [8, 28], to further unravel the mechanisms of how REEP1 prevents MN loss in G93A mice, we next determined the expression of REEP1 in the ER and mitochondria-enriched fractions from the spinal cord of G93A mice. Immunoblot results demonstrated that REEP1 expression decreased in both ER and mitochondrial fractions (Fig.

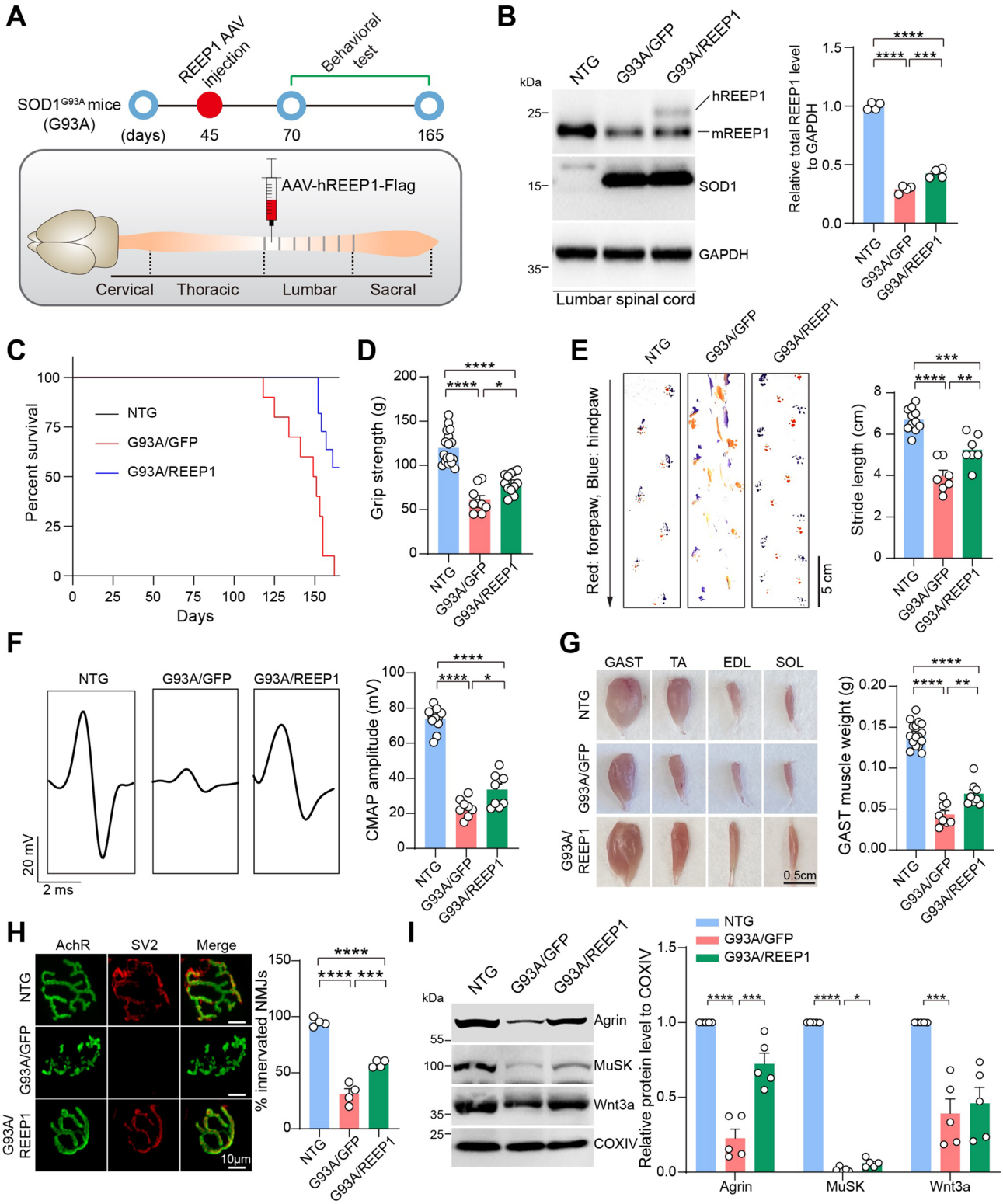

S4A), indicating that loss of expression of REEP1 is probably associated with ER and mitochondrial dysfunction in G93A mice. To investigate the effect of REEP1 on mitochondria, we generated REEP1-knockout Lenti-X 293T cells (REEP1-KO) (Fig. 4A) and evaluated mitochondrial function. We first determined the mitochondrial morphology and distribution in REEP1-KO cells by staining mitochondria with anti-TOM20 antibodies. In >95% of the WT cells, mitochondria with similar sizes were distributed uniformly throughout the cell (Fig. 4B). However, in 41% of REEP1-KO cells mitochondria

◂**Fig. 2** REEP1 upregulation improves the motor performance of G93A mice. **A** Schematic of REEP1 AAV injection and behavioral test timeline. AAV serotype 1 encoding human REEP1 under the neuron-specific promoter eSYN (AAV1-hREEP1-Flag) was injected into the spinal cord at the first lumbar segment (L1) of G93A mice. **B** Representative immunoblots and quantification of REEP1 levels in the lumbar spinal cord of NTG, G93A/GFP, and G93A/REEP1 mice (n = 4 mice per group). **C** Kaplan-Meier survival curves of NTG (n = 16), G93A/GFP (n = 10), and G93A/REEP1 mice (n = 11). **D** Hindlimb grip strength of NTG (n = 17), G93A/GFP (n = 9), and G93A/REEP1 mice (n =12) at 100 days old. **E** Footprint performance and stride length quantification of NTG (n = 11), G93A/GFP (n = 7), and G93A/REEP1 mice (n = 7). The arrow shows the direction of walking. **F** Representative images and quantification of CMAPs evoked by supramaximal stimulation of the sciatic nerve in NTG (n = 12), G93A/GFP (n = 8), and G93A/REEP1 mice (n = 9). **G** Representative images of skeletal muscles and quantification of gastrocnemius muscle weight of NTG (n = 16), G93A/GFP (n = 8), and G93A/REEP1 mice (n = 8). Scale bar, 0.5 cm. **H** Representative images and quantification of NMJ innervation of NTG, G93A/GFP, and G93A/REEP1 mice (n = 4 mice per group). Green, acetylcholine receptors (AchR) stained by α-bungarotoxin for motor endplates; red, SV2 for NMJs. Scale bars, 10 μm. **I** Representative immunoblots and quantification of Agrin, Wnt3a, and MuSK in gastrocnemius muscle of NTG, G93A/GFP, and G93A/REEP1 mice (n = 5 mice per group). Data are the mean ± SEM. *P <0.05, **P <0.01, ***P <0.001, ****P <0.0001, one-way ANOVA followed by Tukey's multiple comparisons test (**B, D, E–I**).

were aggregated around the perinuclear area, indicating that loss of REEP1 expression induces mitochondrial aggregation (Fig. 4B). Since abnormal distribution is always linked to mitochondrial dysfunction, we further assessed the mitochondrial membrane potential by TMRM staining in live cells, and found that REEP1-KO cells showed a dramatically decreased mitochondrial membrane potential (Fig. 4C). Consistent with this, we also found a reduction of intracellular ATP levels in REEP1-KO cells (Fig. 4D). To study the mechanism underlying the ATP reduction in REEP1-KO cells, we used both native and denaturing electrophoresis to examine mitochondrial OXPHOS assembly. Although no changes were noted in the expression of five complex markers (Fig. S4B), both the assembly and activity of CIV were impaired in REEP1-KO cells (Fig. 4E, F). Similar results were obtained in REEP1-knockout M17 cells, a human neuroblastoma cell line (Fig. S4C). Consistent with this, CIV showed drastically decreased assembly in G93A mice when compared to NTG control (Figs 4G and S4D). Together, these data suggest that REEP1 deficiency suppresses mitochondrial functions.

Meanwhile, the impact of the reduction of REEP1 expression on cell proliferation was also examined. Compared with WT cells, REEP1-KO cells had a significantly decreased proliferation rate (Fig. 4H). As REEP1 is closely associated with not only mitochondrial function but also ER function [8, 28], we hypothesized that the impaired proliferation of REEP1-KO cells may be due to either ER or mitochondrial dysfunction. However, ER structures with an interconnected network of branching tubules in REEP1-KO cells were almost identical to WT cells (Fig. S4E). In addition, previous studies have shown that REEP1 plays a role in ER stress resistance [29, 30]. We then examined the level of the ER stress signaling marker phosphorylated eIF2α (p-eIF2α) in WT and REEP1-KO cells. Immunoblot analysis showed that the p-eIF2α levels in REEP1-KO cells were comparable to those in WT cells, suggesting there is no ER-stress response ongoing in REEP1-depleted cells (Fig. S4F). Altogether, these data support the conclusion that the decreased proliferation of REEP1-KO cells is likely caused by impaired mitochondrial functions.

REEP1 Interacts with CIV Subunits

Although previous studies have shown that REEP1 is localized in mitochondria [8], the specific localization in mitochondria remains unclear. To address this question, Lenti-X 293T cells were co-transfected with Mito-OMM-GFP and REEP1-Flag, and immunofluorescence staining was applied. After image deconvolution, the immunofluorescent signals from REEP1-Flag co-localized with the co-expressed outer mitochondrial membrane marker Mito-OMM-GFP. Interestingly, part of the REEP1-Flag signal was surrounded by Mito-OMM-GFP, suggesting that REEP1 is also localized inside mitochondria (Fig. S5A). In an attempt to investigate the localization of REEP1 in mitochondria, we prepared submitochondrial compartments by separating the outer mitochondrial membrane (OMM), inner mitochondrial membrane (IMM), mitochondrial intermembrane space (IMS), and matrix from purified mitochondria. Immunoblot analysis revealed that REEP1 was present in both the OMM and IMM fractions (Fig. 5A). Together, these data support the conclusion that REEP1 is localized in the OMM and IMM.

To explore the function of mitochondrial membrane-associated REEP1, a quantitative mass spectrometry (MS)-based approach was used to monitor the dynamics of REEP1-associated protein complexes (Fig. S5B). 82 proteins were found to be enriched in the pull-down samples from the REEP1-Strep-expressing Lenti-X 293T cells (Table. S1). Kyoto Encyclopedia of Genes and Genomes analysis showed that these proteins were enriched in many neurodegenerative diseases, such as Parkinson's disease and Huntington's disease, strongly supporting the idea that these defects in REEP1-regulated pathways could be a common mechanism of neurodegeneration (Fig. S5C). Consistent with the previous study, Gene Oncology analysis revealed that these proteins are mainly localized in membrane structures, including ER and mitochondria (Fig. S5D). Interestingly, we found that these proteins were commonly enriched in Gene Ontology terms largely related to membrane organization and mitochondrial ATP synthesis-coupled proton transport (Figs 5B and S5E). Among these proteins, 5 OXPHOS subunits belonging to CIV and CV were identified: NDUFA4, ATP5A1, ATP5B,

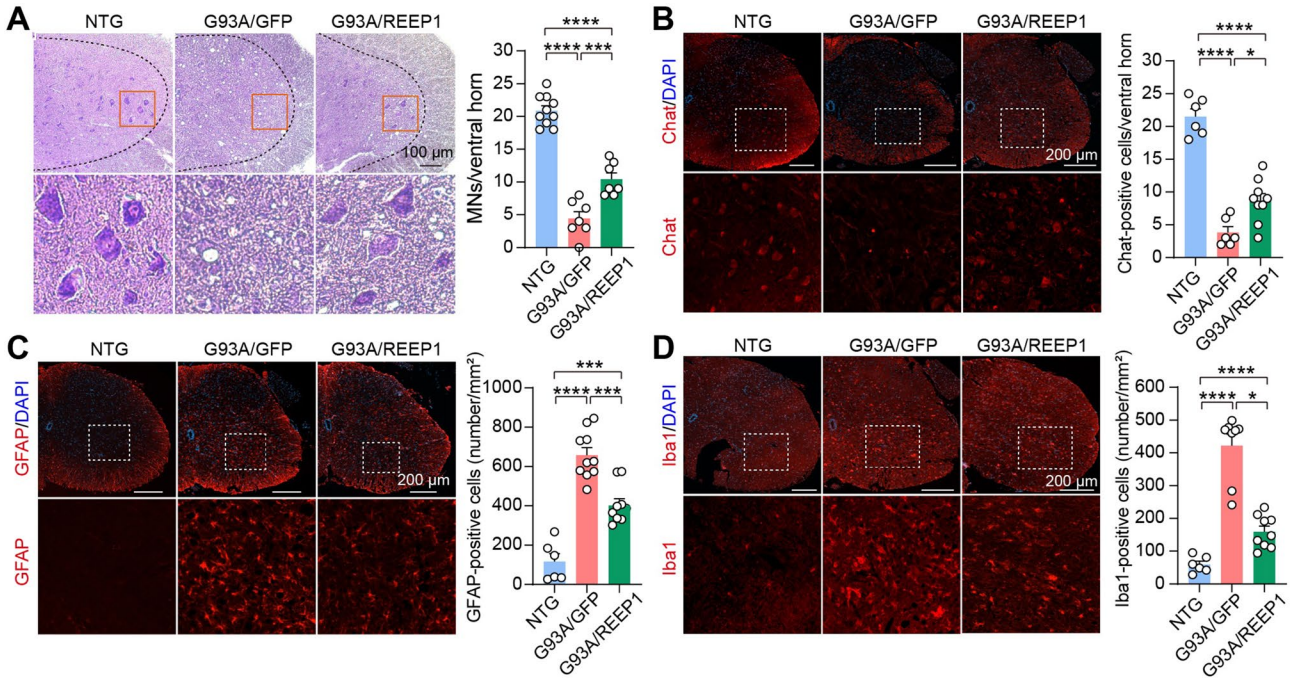

Fig. 3 REEP1 augmentation prevents neuronal loss and gliosis in G93A mice. **A** Representative images and quantification of Nissl staining in the spinal cord of NTG (n = 10), G93A/GFP (n = 7), and G93A/REEP1 mice (n = 7). Scale bar, 100 μm. **B** Representative images and quantification of immunofluorescence staining of Chat in the spinal cord of NTG (n = 6), G93A/GFP (n = 6), and G93A/REEP1 mice (n = 9). Scale bars, 200 μm. **C** Representative images and quantification of immunofluorescence staining of GFAP in the spinal cord of NTG (n = 6), G93A/GFP (n = 10), and G93A/REEP1 mice (n = 9). Scale bars, 200 μm. **D** Representative images and quantification of immunofluorescence staining of Iba1 in the spinal cord of NTG (n = 6), G93A/GFP (n = 8), and G93A/REEP1 mice (n = 9). Scale bars, 200 μm. Data are the mean ± SEM. *P <0.05, ***P <0.001, ****P <0.0001, one-way ANOVA followed by Tukey's multiple comparisons test.

ATP5F, and ATP5O. Co-immunoprecipitation (co-IP) analysis further validated the interaction between REEP1 and NDUFA4, ATP5O, and ATP5A1 co-immunoprecitation between transfected exgenously-expressed NDUFA4-GFP and REEP1 WT/REEP1Δ101–110.

To further assess the importance of the REEP1 and NDUFA4 association on CIV assembly, we generated a series of deletion mutations of REEP1 and analyzed their interaction with NDUFA4 (Fig. 5D). We tagged REEP1 at the C-terminus with Strep-tag and co-IP was applied by using cell lysates from NDUFA4-GFP and truncated REEP1-Strep co-transfected Lenti-X 293T cells. A 140 amino-acid (aa) deletion in the N-terminal region of REEP1 abolished the interaction between REEP1 and NDUFA4. On the other hand, deletion of N-terminal 100 aa (ΔN100) remarkably increased the association of REEP1 with NDUFA4 (Fig. 5E). Although further immunofluorescence and subcellular fraction analysis demonstrated that ΔN100 was present in both the ER and mitochondria, more ΔN100 was enriched in the mitochondrial fraction than full-length REEP1 (Fig. S5H, I). This is consistent with a previous study showing that the loss of the N-terminal domain of REEP1 greatly increased its mitochondrial distribution [31]. We then generated truncated mutations between 100 aa and 140 aa of REEP1. Co-IP analysis showed that the removal of the N-terminal 110 aa (ΔN110) disrupted the interaction between REEP1 and NDUFA4 (Fig. 5F). Like the REEP1ΔN110 (deletion of the N-terminal 110 aas), the REEP1Δ101–110, which lacked the 10 aa residues from 101 to 110, completely abrogated the ability of REEP1 to co-precipitate with NDUFA4 (Fig. 5G). The above results suggest that 101–110 aa of REEP1 is necessary for its binding to NDUFA4.

REEP1 Regulates CIV Assembly Through Interaction with NDUFA4

Based on the identification of the 101–110 motif required for interactions between REEP1 and NDUFA4, we next performed rescue experiments in REEP1-KO cells to validate their functional role in maintaining mitochondrial function. We first explored the subcellular localization of the REEP1Δ101–110 by isolation of ER and pure mitochondria

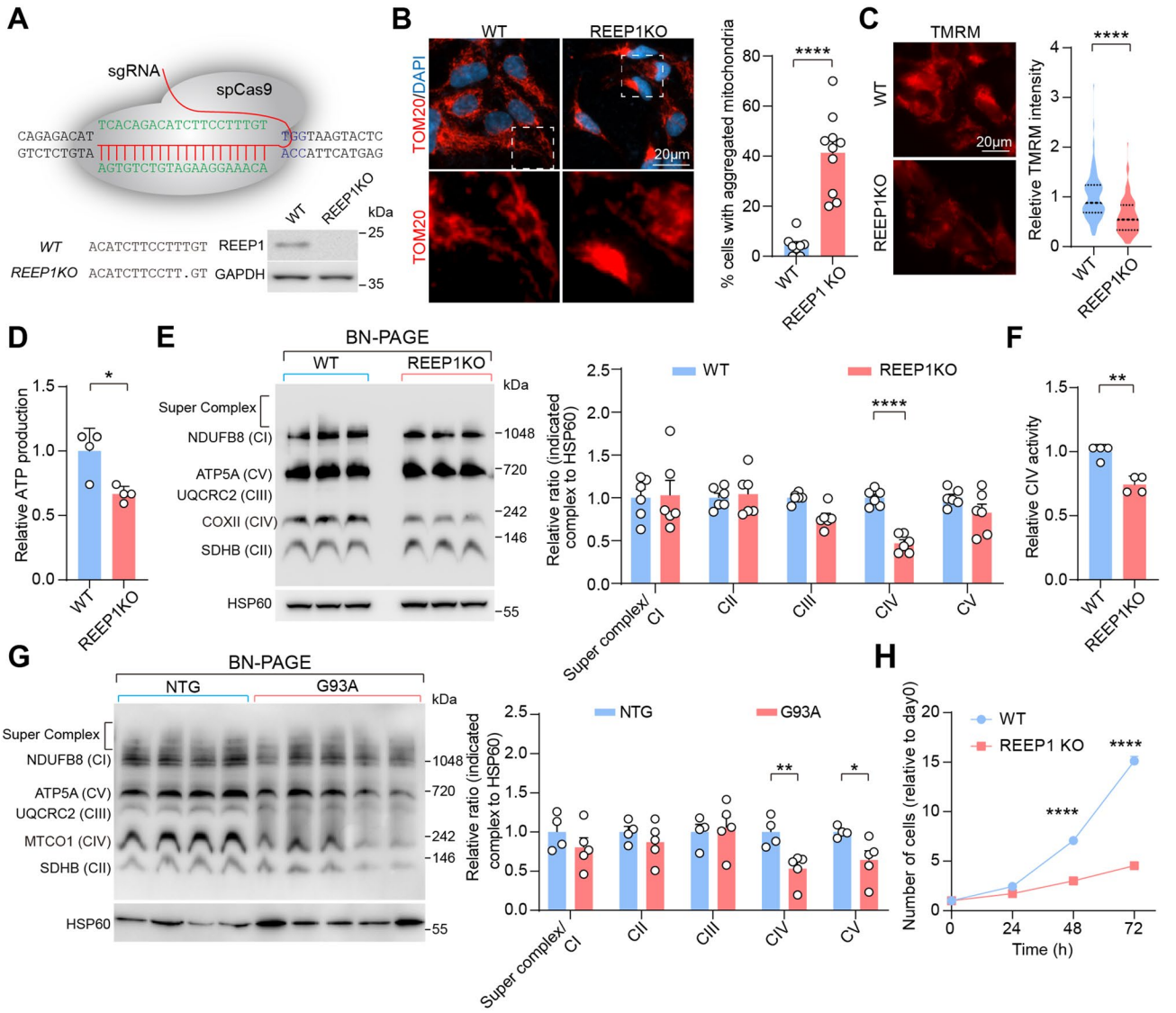

Fig. 4 Loss of REEP1 impairs mitochondrial function. **A** Schematic of CRISPR/Cas9 genome-editing of the REEP1 gene in Lenti-X 293T cells to obtain REEP1-KO cells validated by western blot and DNA sequencing analysis. GAPDH was used as the loading control. **B** Representative images and quantification of aggregated mitochondria in WT (n = 191 cells from 3 experiments) and REEP1-KO cells (n = 178 cells from 3 experiments). Mitochondria are stained with TOM20. DAPI to visualize nuclei. Scale bar, 20 μm. **C** Quantification of mitochondrial membrane potential staining by TMRM in WT (n = 101 cells from three experiments) and REEP1KO cells (n = 111 cells from three experiments). Scale bar, 20 μm. **D** Quantification of ATP levels in WT and REEP1-KO cells (n = 4 replicates). **E** Representative immunoblots and quantification of mitochondrial OXPHOS assembly in WT and REEP1-KO cells (n = 6 replicates). **F** Quantification of mitochondrial CIV activity in WT and REEP1-KO cells (n = 4 replicates). **G** Representative immunoblots and quantification of mitochondrial OXPHOS assembly in 120-day-old NTG (n = 4) and G93A mice (n = 5). **H** Growth curves for WT and REEP1KO cells over 72 h. Data are the mean ± SEM. *P <0.05, **P <0.01, ****P <0.0001, two-tailed Student's t-test (**B–G**) and two-way ANOVA followed by Bonferroni multiple comparisons test (**H**).

(Fig. 6A). Similar to WT REEP1, REEP1Δ101–110 was present in both ER and mitochondrial fractions, implying that loss of this motif did not change the subcellular localization of REEP1. Then, cell proliferation and mitochondrial function were analyzed to determine whether the loss of the interaction between REEP1 and NDUFA4 could rescue the phenotype caused by REEP1-knockout. Overexpression of WT REEP1, but not the Δ101–110 mutations, restored the proliferation deficiency of REEP1-KO cells (Fig. S6A). Unexpectedly, REEP1-KO cells expressing either REEP1 or REEP1Δ101–110 showed similar mitochondrial distribution, suggesting that the changes in mitochondrial

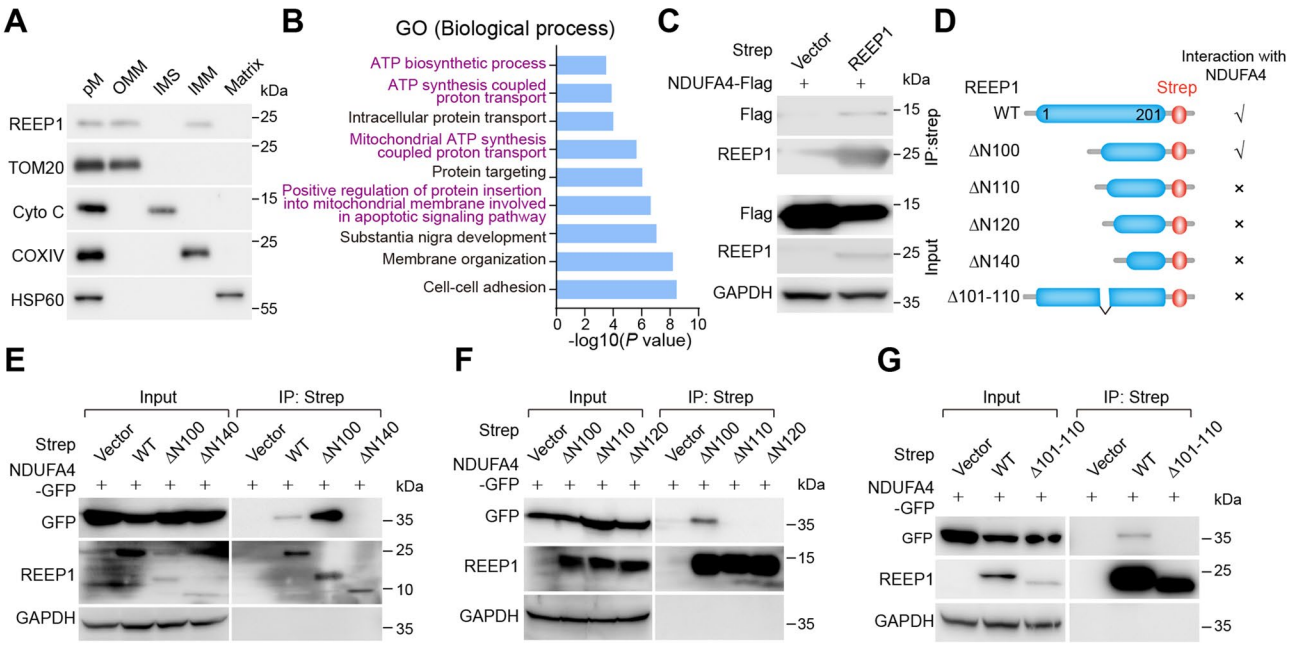

Fig. 5 REEP1 interacts with NDUFA4. **A** Representative immunoblots of REEP1 and markers for sub-mitochondrial fractions from Lenti-X 293T cells: TOM20 for the outer mitochondrial membrane, Cyto C for the inner membrane space of mitochondria, COXIV for the inner mitochondrial membrane, and HSP60 for the mitochondrial matrix. **B** Gene Ontology enrichment analysis of unique interactors of REEP1 according to categories based on biological process. **C** Representative immunoblots of co-immunoprecipitation between transfected REEP1-Strep and NDUFA4-Flag in Lenti-X 293T cells. **D** Schematic of REEP1 deletion mutants used for mapping the binding site for NDUFA4. **E, F** Representative immunoblots of co-immunoprecitation between transfected exgenously-expressed NDUFA4-GFP and REEP1 WT/REEP1Δ101–110.

distribution caused by REEP1 loss are not dependent on the interaction between REEP1 and NDUFA4 (Fig. 6B). Moreover, mitochondrial membrane potential and intracellular ATP levels were rescued in REEP1-KO cells expressing REEP1, but not in cells expressing Δ101–110 (Figs 6C, D and S6B). In addition, CIV assembly and activity were also restored by overexpression of REEP1, but not Δ101–110 REEP1 (Fig. 6E, F). Therefore, our results strongly suggest that the interaction between REEP1 and NDUFA4 is necessary for maintaining normal mitochondrial function.

As NDUFA4 is essential for CIV assembly and activity, we next studied the expression of NDUFA4 in G93A mice and REEP1-KO cells. Immunoblot analysis revealed that NDUFA4 expression was greatly reduced in the spinal cord of 120-day-old G93A mice compared with age-matched NTG mice (Fig. 6G). Consistent with this, NDUFA4 levels were significantly decreased in REEP1-KO (both Lenti-X 293T cells and M17 cells) (Figs 6H and S6C). While REEP1 completely restored the expression of NDUFA4 in REEP1-KO cells, Δ101–110 REEP1-expressing REEP1-KO cells revealed levels of NDUFA4 similar to REEP-KO cells (Fig. 6H). As no NDUFA4 mRNA levels change occurred in these cells (Fig. 6I), REEP1 is likely involved in NDUFA4 degradation. Together, these data support the conclusion that REEP1 is an important regulator of CIV assembly through interaction with NDUFA4.

To further validate these findings in neuronal cells, we generated REEP1-KO SH-SY5Y cells and restored REEP1 expression in these cells by re-expressing WT REEP1 and REEP1 Δ101–110. These stable cell lines were further differentiated into neurons, which were used for mitochondrial function analysis and neuronal survival assay (Fig. S7A–H). Consistent with the results from Lenti-X 293T cells, re-expressing REEP1 restored NDUFA4 expression and the CIV defects in REEP1-KO neurons. However, neurons expressing REEP1Δ101–110 had NDUFA4 levels and CIV defects similar to REEP1-KO neurons, suggesting that the interaction between REEP1 and NDUFA4 is critical for mitochondrial function in neuronal cells (Fig. S7C, D). Although the loss of REEP1 did not affect neuronal survival, REEP1-KO neurons had shorter branches than WT neurons, indicating that REEP1 is essential for neurite outgrowth during neuronal differentiation (Fig. S7E–G). Previous studies have reported that SOD1G93A overexpression induces both oxidative stress and ER stress in neuronal cells, and this potently contributes to neuronal death [32, 33]. To explore the importance of REEP1 for neuronal survival

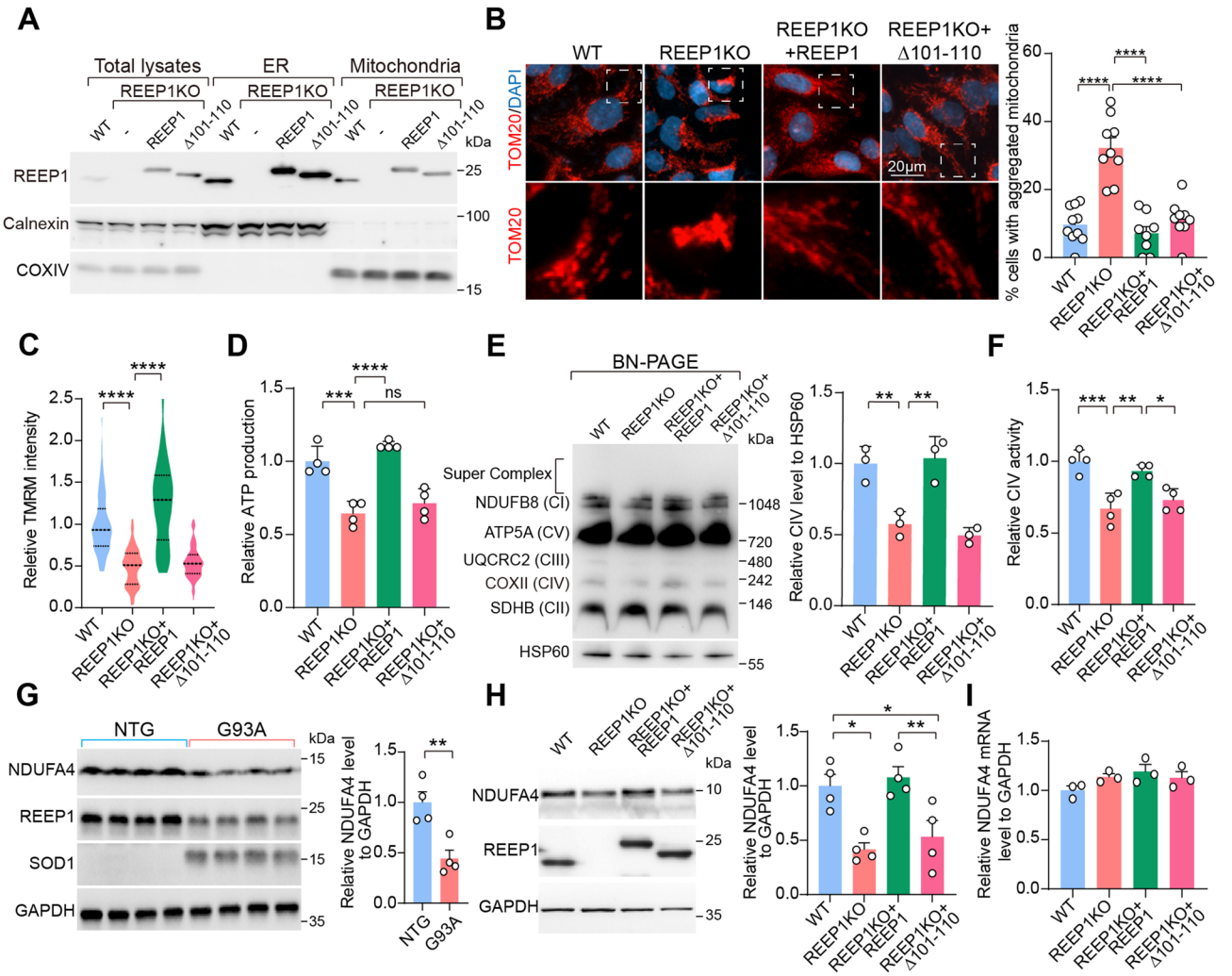

Fig. 6 REEP1 regulates CIV assembly through interaction with NDUFA4. **A** Representative immunoblots of REEP1 in the ER and mitochondrial fractions of indicated cells. Calnexin and COXIV were used as ER and mitochondrial markers, respectively. Overexpressed REEP1 WT and REEP1Δ101–110 carrying Strep-tag. **B** Representative images and quantification of aggregated mitochondria in WT (n = 192 cells from 3 experiments), REEP1KO (n = 210 cells from 3 experiments), REEP1KO+REEP1 (n = 218 cells from 3 experiments), and REEP1-KO+Δ101–110 cells (n = 169 cells from 3 experiments). Mitochondria are stained by TOM20. DAPI is used to visualize nuclei. Scale bar, 20 μm. **C** Quantification of mitochondrial membrane potential staining by TMRM in WT (n = 99 cells from 3 experiments), REEP1-KO (n = 82 cells from 3 experiments), REEP1-KO+REEP1 (n = 94 cells from 3 experiments), and REEP1-KO+Δ101–110 cells (n = 104 cells from 3 experiments). **D** Quantification of ATP levels in WT, REEP1-KO, REEP1-KO+REEP1, and REEP1-KO+Δ101–110 cells (n = 4 replicates). **E** Representative immunoblots and quantification of mitochondrial OXPHOS assembly in WT, REEP1-KO, REEP1-KO+REEP1, and REEP1-KO+Δ101–110 cells (n = 3 replicates). **F** Quantification of mitochondrial CIV activity in WT, REEP1-KO, REEP1-KO+REEP1, and REEP1-KO+Δ101–110 cells (n = 4 replicates). **G** Representative immunoblots and quantification of NDUFA4 expression in the spinal cord from 120-day-old NTG and G93A mice (n = 4 mice per group). **H** Representative immunoblots and quantification of NDUFA4 expression in WT, REEP1-KO, REEP1-KO+REEP1, and REEP1-KO+Δ101–110 cells (n = 4 replicates). **I** Relative mRNA levels of NDUFA4 in WT, REEP1-KO, REEP1-KO+REEP1, and REEP1-KO+Δ101–110 cells (n = 3 replicates). Data are the mean ± SEM. $^*P$ <0.05, $^{**}P$ <0.01, $^{***}P$ <0.001, $^{****}P$ <0.0001, two-tailed Student's t-test (G) and one-way ANOVA followed by Tukey's multiple comparisons test (**B–F, H**, and **I**).

under stress conditions, we treated SH-SY5Y-derived neurons with H_2O_2 and Tunicamycin (TM) to induce oxidative stress and ER stress, respectively (Fig. S7H). Strikingly, loss of REEP1 caused greatly increased sensitivity to oxidative stress in neuronal cells. And re-expressing WT REEP1, but not REEP1Δ101–110, fully protected REEP1-KO cells from oxidative stress compared with WT neurons. Similar phenomena were also found in TM-treated neurons (Fig. S7H). These data together suggest that REEP1 and its interaction with NDUFA4 are critical for neuronal survival under stress conditions.

Mitochondrial Abnormalities in G93A Mice are Restored by REEP1 Upregulation

Next, we determined whether the protective effect mediated by REEP1 augmentation in G93A mice was through mitochondria-associated pathways by analyzing mitochondrial morphology and function in NTG, G93A/GFP, and G93A/REEP1 mice. Although there was a significant upregulation of REEP1 protein levels in lumbar spinal cord extracts from G93A/REEP1 mice compared to G93A/GFP mice, the expression of REEP1 in G93A/REEP1 mice was still lower than that in NTG mice (Fig. 2B). Unexpectedly, immunoblot analysis revealed that reduction of REEP1 expression in the mitochondria of G93A mice was fully restored by AAV1-hREEP1-Flag injection (Fig. 7A). Moreover, the reduced expression of NDUFA4 was partially rescued in lumbar spinal cord extracts from G93A/REEP1 mice (Fig. 7B). Despite that no morphological changes in the ER were noted in these mice, mitochondria in the MNs of G93A mice became fragmented as evidenced by the decrease in mitochondrial length, which was restored by forced expression of REEP1 (Figs. 7C and S8A). Although there were no statistically significant differences, the mitochondrial membrane potential in G93A/REEP1 mice had an increasing trend compared to G93A/GFP mice (Fig. S8B). Activity analysis also demonstrated that CIV deficiencies were rescued by REEP1 upregulation (Fig. 7D). These findings further support the idea that REEP1 protects MNs by improving mitochondrial functions.

Discussion

Here we showed that the expression of REEP1 is significantly reduced in the spinal cord of G93A mice. Augmentation of REEP1 preserved the motor performance of G93A mice by improving mitochondrial function. On the mechanistic level, we demonstrated that REEP1 regulates mitochondrial CIV assembly by association with NDUFA4. These findings partially explain that the mitochondrial CIV dysfunction in ALS and other neurodegenerative diseases might be associated with REEP1 loss-of-function (Fig. 7E).

Morphological alterations of membrane-bound organelles, such as ER, mitochondria, and Golgi have been consistently reported in ALS patients and ALS-associated mouse models [34–39]. As a membrane curvature-inducing protein with various subcellular localizations, our findings suggest that REEP1 deficiency may be responsible for the morphological changes of mitochondria, but not ER structure, in ALS and its experimental models. Since the expression of other REEPs is not altered, REEP1 deficiency is likely specific to ALS. In addition, experimental models without REEP1 expression demonstrate abnormalities in the ER and mitochondrial morphogenesis [11, 28]. All these studies together suggest that REEP1-mediated dysfunction of organelles might be the cause rather than the consequence of ALS. It is still unclear why mRNA of REEP1 decreases in ALS and it would be interesting to investigate the essential factors regulating REEP1 expression at the transcriptional level.

Regarding the subcellular localization of REEP1, conflicting results have been reported. Although REEP1 was initially identified as a mitochondrial membrane protein [8], later studies showed that endogenous REEP1 is localized to the ER [7, 12, 40]. It is not clear whether this discrepancy is due to the differences in antibody specificity or differences in cell types. Recently, one study has proposed that REEP1 contains subdomains for both mitochondrial and ER localization. The N-terminal domain (aas 1–115) of REEP1 has been shown to facilitate ER localization, whereas the middle domain (aas 116–157) promotes mitochondrial localization [28]. Our findings in this study suggested that REEP1 is located in the inner mitochondrial membrane, forms a protein complex with CIV, and stabilizes the CIV subunit NDUFA4. Of note, no changes were found in CV assembly in REEP1-KO cells, although several subunits have been shown to interact with REEP1, indicating multiple roles of REEP1 in OXPHOS complexes. Further studies are needed to explore the functional consequences of the interactions between REEP1 and CV subunits.

Besides its IMM localization, immunofluorescence staining and subcellular fraction results also showed that REEP1 was present in the OMM (Figs. 5A and S5A). Consistent with this, OMM components associated with REEP1 were also identified by mass spectrometry analysis, including VDAC1, VDAC2, and VDAC3 (Table S1). These data imply that REEP1 may be involved in regulating metabolic and energetic flux across the OMM. More interestingly, the re-expression of REEP1Δ101–110 entirely rescued perinuclear mitochondrial aggregation in REEP1-KO cells, suggesting that REEP1 regulates mitochondrial distribution through a pathway distinct from IMM REEP1-mediated CIV assembly. In mammalian cells, mitochondrial distribution is dependent on the microtubule cytoskeleton and a previous study has demonstrated that the REEP1 C-terminal cytoplasmic domain is essential for the interaction with microtubules [7, 41]. Since the microtubule-binding motif is intact in REEP1Δ101–110 mutation, OMM-localized REEP1 likely controls mitochondrial distribution in a microtubule-dependent manner. It will be intriguing to explore the role of OMM-REEP1 in the regulation of mitochondrial morphology.

In addition to changes in mitochondrial morphology, respiratory chain deficiency has been extensively reported in patients and animal models of ALS and has been implicated to be directly involved in disease pathogenesis. Among

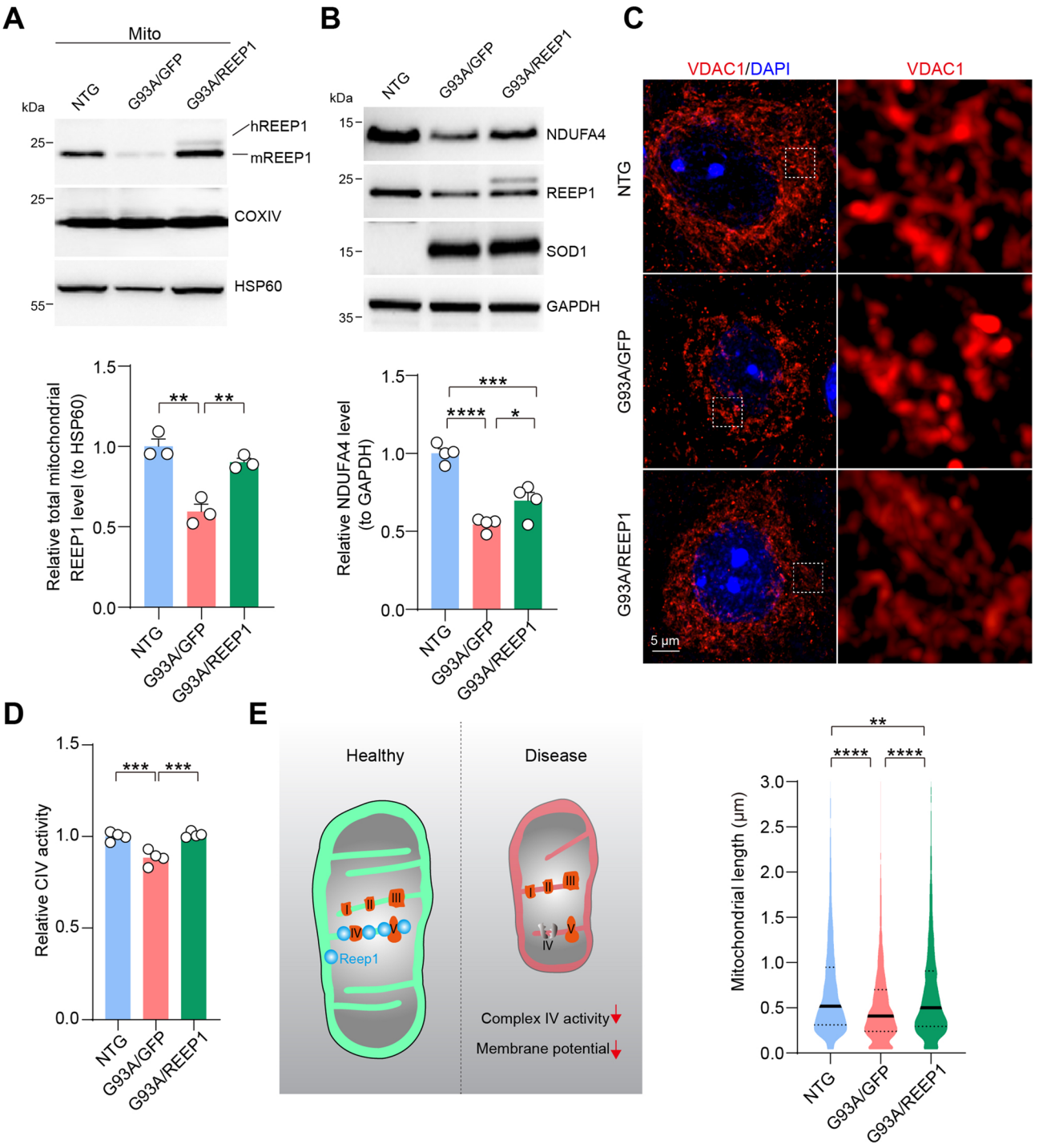

Fig. 7 Impaired mitochondrial function in G93A mice is restored by REEP1 upregulation. **A** Representative immunoblots and quantification of REEP1 levels in mitochondrial fractions from the lumbar spinal cord of NTG, G93A/GFP, and G93A/REEP1 mice (n = 3 mice per group). **B** Representative immunoblots and quantification of NDUFA4 levels in the lumbar spinal cord of NTG, G93A/GFP, and G93A/REEP1 mice (n = 4 mice per group). **C** Representative images and quantification of the mitochondrial length in motor neurons from NTG, G93A/GFP, and G93A/REEP1 mice (n = 10–15 cells from 3 mice per group). Scale bar, 5 μm. **D** Quantification of CIV activity of mitochondria from NTG, G93A/GFP, and G93A/REEP1 mice (n = 4 mice per group). **E** Schematic of mitochondrial dysfunction caused by REEP1 deficiency. Under healthy conditions, REEP1 is localized in the outer and inner mitochondrial membranes, where it maintains OXPHOS assembly through interaction with its subunits. In the mitochondria of ALS patients, the reduction of REEP1 expression causes mitochondrial CIV disassembly and membrane potential loss. Data are the mean ± SEM. *P <0.05, **P <0.01, ***P <0.001, ****P <0.0001, one-way ANOVA followed by Tukey's multiple comparisons test (**A–D**).

ALS-associated proteins, mutant SOD1 causes not only mitochondrial dynamic changes but also a reduction of OXPHOS assembly and activity [42, 43]. The presence of SOD1G93A in NSC34 cells leads to a significant decrease in the activities of CII and CIV [44]. Consistent with this, in the spinal cord of sporadic ALS cases, CIV activity is markedly reduced [45]. All these data strongly support the idea that CIV deficiency is a distinguishing feature of patients and mouse models of ALS. In this study, we found that overexpression of human REEP1 in G93A mice, which shares 98% similarity with mouse REEP1, improved CIV activity. On the other hand, loss of REEP1 disturbed CIV function, which is essential for cell proliferation in dividing Lenti-X 293T cells. Consistent with this, a reduction of CIV activity was also found in REEP1-KO neurons, suggesting that REEP1 plays a key role in the regulation of CIV function in both dividing and non-dividing cells. Although the loss of REEP1 did not affect neuronal survival under physiological conditions, REEP1-KO neurons demonstrated greatly increased sensitivity to oxidative stress and ER stress. As oxidative stress and mitochondrial dysfunction are detrimental to neuron survival in G93A mice, our data strongly suggest that reduction of REEP1 in the motor neuron may play a central role in motor neuron degeneration in patients and animal models of ALS.

NDUFA4 was first identified as a constituent of NADH dehydrogenase (CI), although later studies revealed that it is a component of CIV and plays a critical role in the assembly and biogenesis of CIV, rather than CI [46, 47]. Our findings revealed that NDUFA4 reduction is a predominant feature of G93A mice. As the mRNA level did not change, the protein level changes of NDUFA4 probably depend on its degradation. The highly heterogeneous lifespans of individual OXPHOS subunits are mainly controlled by the mitochondrial proteolysis system. Mitochondrial proteases facilitate the precise surveillance, removal, and repair of damaged or redundant OXPHOS complexes [48]. The interaction between NDUFA4 and REEP1 might block mitochondrial protease access to the proteolysis sites of NDUFA4. In future studies, the potential proteases for NDUFA4 degradation should be identified, and their role in ALS and other neurodegenerative diseases needs to be explored.

Impaired mitochondrial bioenergetics has been considered to be an important and potential therapeutic target for many neurodegenerative diseases. Many studies have already demonstrated the feasibility of using small molecules to improve mitochondrial OXPHOS activity as a novel approach to prevent neuronal loss and even improve behaviors in experimental models of ALS and Parkinson's disease. For example, one most recent study showed that R13 treatment ameliorates the decline in motor symptoms and associated pathological changes in G93A mice by enhancing the expression level of OXPHOS-related proteins and accelerating mitochondrial biogenesis [49]. In addition, the small molecule-targeting succinate dehydrogenase subunit B (SDHB) protein of CII blocks dopaminergic neuron death and reverses the behavioral deficits in a rat model of Parkinson's disease [50]. Our data also demonstrated that improvement of mitochondrial CIV assembly and activity greatly alleviated motor neuron death and behavioral deficits in G93A mice. All these studies support the hypothesis that targeting mitochondrial bioenergetics may be a common therapeutic approach to improve mitochondrial and neuronal functions and prevent neurodegeneration.

As discussed above, the REEP1 deficiency described in this study in ALS and ALS mouse models is likely an important mediator of impaired mitochondrial morphology and function in ALS. The REEP1-NDUFA4 axis might be a potential novel therapeutic approach worthy of continued investigation and validation in other experimental models.

Acknowledgements This work was supported by Shandong Key R & D Program Funding (2018GSF118037) and the Shandong Natural Science Foundation (ZR2019JQ24). We thank Translational Medicine Core Facility of Shandong University for consultation and instrument availability that supported this work.

Conflict of interest The authors declare that there are no conflicts of interest.

References

1. Hao Z, Wang R, Ren H, Wang G. Role of the *C9ORF72* gene in the pathogenesis of amyotrophic lateral sclerosis and frontotemporal dementia. Neurosci Bull 2020, 36: 1057–1070.
2. Wiedemann FR, Manfredi G, Mawrin C, Beal MF, Schon EA. Mitochondrial DNA and respiratory chain function in spinal cords of ALS patients. J Neurochem 2002, 80: 616–625.
3. Borthwick GM, Johnson MA, Ince PG, Shaw PJ, Turnbull DM. Mitochondrial enzyme activity in amyotrophic lateral sclerosis: Implications for the role of mitochondria in neuronal cell death. Ann Neurol 1999, 46: 787–790.
4. Mattiazzi M, D'Aurelio M, Gajewski CD, Martushova K, Kiaei M, Beal MF. Mutated human SOD1 causes dysfunction of oxidative phosphorylation in mitochondria of transgenic mice. J Biol Chem 2002, 277: 29626–29633.
5. Saito H, Kubota M, Roberts RW, Chi Q, Matsunami H. RTP family members induce functional expression of mammalian odorant receptors. Cell 2004, 119: 679–691.
6. Behrens M, Bartelt J, Reichling C, Winnig M, Kuhn C, Meyerhof W. Members of *RTP* and REEP gene families influence functional bitter taste receptor expression. J Biol Chem 2006, 281: 20650–20659.
7. Park SH, Zhu PP, Parker RL, Blackstone C. Hereditary spastic paraplegia proteins REEP1, spastin, and atlastin-1 coordinate microtubule interactions with the tubular ER network. J Clin Invest 2010, 120: 1097–1110.
8. Züchner S, Wang G, Tran-Viet KN, Nance MA, Gaskell PC, Vance JM, *et al*. Mutations in the novel mitochondrial protein REEP1 cause hereditary spastic paraplegia type 31. Am J Hum Genet 2006, 79: 365–369.

9. Beetz C, Schüle R, Deconinck T, Tran-Viet KN, Zhu H, Kremer BPH, *et al*. REEP1 mutation spectrum and genotype/phenotype correlation in hereditary spastic paraplegia type 31. Brain 2008, 131: 1078–1086.
10. Goizet C, Depienne C, Benard G, Boukhris A, Mundwiller E, Solé G, *et al*. REEP1 mutations in SPG31: Frequency, mutational spectrum, and potential association with mitochondrial morpho-functional dysfunction. Hum Mutat 2011, 32: 1118–1127.
11. Renvoisé B, Malone B, Falgairolle M, Munasinghe J, Stadler J, Sibilla C, *et al*. Reep1 null mice reveal a converging role for hereditary spastic paraplegia proteins in lipid droplet regulation. Hum Mol Genet 2016, 25: 5111–5125.
12. Beetz C, Koch N, Khundadze M, Zimmer G, Nietzsche S, Hertel N, *et al*. A spastic paraplegia mouse model reveals REEP1-dependent ER shaping. J Clin Invest 2013, 123: 4273–4282.
13. Falk J, Rohde M, Bekhite MM, Neugebauer S, Hemmerich P, Kiehntopf M, *et al*. Functional mutation analysis provides evidence for a role of REEP1 in lipid droplet biology. Hum Mutat 2014, 35: 497–504.
14. Klemm RW Jr, Norton JP, Cole RA, Li CS, Park SH, Crane MM, *et al*. A conserved role for atlastin GTPases in regulating lipid droplet size. Cell Rep 2013, 3: 1465–1475.
15. Beetz C, Pieber TR, Hertel N, Schabhuttl M, Fischer C, Trajanoski S, *et al*. Exome sequencing identifies a *REEP1* mutation involved in distal hereditary motor neuropathy type V. Am J Hum Genet 2012, 91: 139–145.
16. Wang L, Gao J, Liu JY, Siedlak SL, Torres S, Fujioka H, *et al*. Mitofusin 2 regulates axonal transport of calpastatin to prevent neuromuscular synaptic elimination in skeletal muscles. Cell Metab 2018, 28: 400-414.e8.
17. Ran FA, Hsu PD, Wright J, Agarwala V, Scott DA, Zhang F. Genome engineering using the CRISPR-Cas9 system. Nat Protoc 2013, 8: 2281–2308.
18. Nunomura A, Perry G, Pappolla MA, Wade R, Hirai K, Chiba S, *et al*. RNA oxidation is a prominent feature of vulnerable neurons in Alzheimer's disease. J Neurosci 1999, 19: 1959–1964.
19. Kiser JZ, Post M, Wang B, Miyagi M. *Streptomyces erythraeus* trypsin for proteomics applications. J Proteome Res 2009, 8: 1810–1817.
20. Dravid A, Raos B, Svirskis D, O'Carroll SJ. Optimised techniques for high-throughput screening of differentiated SH-SY5Y cells and application for neurite outgrowth assays. Sci Rep 2021, 11: 23935.
21. Shipley MM, Mangold CA, Szpara ML. Differentiation of the SH-SY5Y human neuroblastoma cell line. J Vis Exp 2016: 53193.
22. Fowler PC, Garcia-Pardo ME, Simpson JC, O'Sullivan NC. NeurodegenERation: The central role for ER contacts in neuronal function and axonopathy, lessons from hereditary spastic paraplegias and related diseases. Front Neurosci 2019, 13: 1051.
23. D'Erchia AM, Gallo A, Manzari C, Raho S, Horner DS, Chiara M, *et al*. Massive transcriptome sequencing of human spinal cord tissues provides new insights into motor neuron degeneration in ALS. Sci Rep 2017, 7: 10046.
24. Vinsant S, Mansfield C, Jimenez-Moreno R, Del Gaizo Moore V, Yoshikawa M, Hampton TG, *et al*. Characterization of early pathogenesis in the SOD1(G93A) mouse model of ALS: Part II, results and discussion. Brain Behav 2013, 3: 431–457.
25. Mancuso R, Osta R, Navarro X. Presymptomatic electrophysiological tests predict clinical onset and survival in SOD1(G93A) ALS mice. Muscle Nerve 2014, 50: 943–949.
26. Koles K, Budnik V. Wnt signaling in neuromuscular junction development. Cold Spring Harb Perspect Biol 2012, 4: a008045.
27. Gurney ME, Pu H, Chiu AY, Dal Canto MC, Polchow CY, Alexander DD, *et al*. Motor neuron degeneration in mice that express a human Cu, Zn superoxide dismutase mutation. Science 1994, 264: 1772–1775.
28. Lavie J, Serrat R, Bellance N, Courtand G, Dupuy JW, Tesson C, *et al*. Mitochondrial morphology and cellular distribution are altered in SPG31 patients and are linked to DRP1 hyperphosphorylation. Hum Mol Genet 2016, 26: 674–685.
29. Appocher C, Klima R, Feiguin F. Functional screening in *Drosophila* reveals the conserved role of REEP1 in promoting stress resistance and preventing the formation of Tau aggregates. Hum Mol Genet 2014, 23: 6762–6772.
30. Wang B, Yu Y, Wei L, Zhang Y. Inhibition of ER stress improves progressive motor deficits in a REEP1-null mouse model of hereditary spastic paraplegia. Biol Open 2020, 9: bio054296.
31. Lim Y, Cho IT, Schoel LJ, Cho G, Golden JA. Hereditary spastic paraplegia-linked REEP1 modulates endoplasmic reticulum/mitochondria contacts. Ann Neurol 2015, 78: 679–696.
32. Nishitoh H, Kadowaki H, Nagai A, Maruyama T, Yokota T, Fukutomi H, *et al*. ALS-linked mutant SOD1 induces ER stress- and ASK_1-dependent motor neuron death by targeting Derlin-1. Genes Dev 2008, 22: 1451–1464.
33. An T, Shi P, Duan W, Zhang S, Yuan P, Li Z, *et al*. Oxidative stress and autophagic alteration in brainstem of SOD1-G93A mouse model of ALS. Mol Neurobiol 2014, 49: 1435–1448.
34. Lautenschlaeger J, Prell T, Grosskreutz J. Endoplasmic reticulum stress and the ER mitochondria calcium cycle in amyotrophic lateral sclerosis. Amyotroph Lateral Scler 2012, 13: 166–177.
35. dal Canto MC, Gurney ME. Neuropathological changes in two lines of mice carrying a transgene for mutant human Cu, Zn *SOD*, and in mice overexpressing wild type human SOD: A model of familial amyotrophic lateral sclerosis (FALS). Brain Res 1995, 676: 25–40.
36. Fujita Y, Okamoto K, Sakurai A, Gonatas NK, Hirano A. Fragmentation of the Golgi apparatus of the anterior horn cells in patients with familial amyotrophic lateral sclerosis with SOD1 mutations and posterior column involvement. J Neurol Sci 2000, 174: 137–140.
37. Stieber A, Gonatas JO, Collard J, Meier J, Julien J, Schweitzer P, *et al*. The neuronal Golgi apparatus is fragmented in transgenic mice expressing a mutant human SOD1, but not in mice expressing the human NF-H gene. J Neurol Sci 2000, 173: 63–72.
38. Oyanagi K, Yamazaki M, Takahashi H, Watabe K, Wada M, Komori T, *et al*. Spinal anterior horn cells in sporadic amyotrophic lateral sclerosis show ribosomal detachment from, and cisternal distention of the rough endoplasmic reticulum. Neuropathol Appl Neurobiol 2008, 34: 650–658.
39. Gao J, Wang L, Liu J, Xie F, Su B, Wang X. Abnormalities of mitochondrial dynamics in neurodegenerative diseases. Antioxidants (Basel) 2017, 6: 25.
40. Hurt CM, Bjork S, Ho VK, Gilsbach R, Hein L, Angelotti T. REEP1 and REEP2 proteins are preferentially expressed in neuronal and neuronal-like exocytotic tissues. Brain Res 2014, 1545: 12–22.
41. Anesti V, Scorrano L. The relationship between mitochondrial shape and function and the cytoskeleton. Biochim Biophys Acta BBA Bioenerg 2006, 1757: 692–699.
42. Magrané J, Hervias I, Henning MS, Damiano M, Kawamata H, Manfredi G. Mutant SOD1 in neuronal mitochondria causes toxicity and mitochondrial dynamics abnormalities. Hum Mol Genet 2009, 18: 4552–4564.
43. Tafuri F, Ronchi D, Magri F, Comi GP, Corti S. SOD1 misplacing and mitochondrial dysfunction in amyotrophic lateral sclerosis pathogenesis. Front Cell Neurosci 2015, 9: 336.
44. Calabria E, Scambi I, Bonafede R, Schiaffino L, Peroni D, Potrich V, *et al*. ASCs-exosomes recover coupling efficiency and mitochondrial membrane potential in an *in vitro* model of ALS. Front Neurosci 2019, 13: 1070.

45. Vielhaber S, Kunz D, Winkler K, Wiedemann FR, Kirches E, Feistner H, *et al*. Mitochondrial DNA abnormalities in skeletal muscle of patients with sporadic amyotrophic lateral sclerosis. Brain 2000, 123(Pt 7): 1339–1348.
46. Carroll J, Fearnley IM, Skehel JM, Shannon RJ, Hirst J, Walker JE. Bovine complex I is a complex of 45 different subunits. J Biol Chem 2006, 281: 32724–32727.
47. Balsa E, Marco R, Perales-Clemente E, Szklarczyk R, Calvo E, Landázuri MO, *et al*. NDUFA4 is a subunit of complex IV of the mammalian electron transport chain. Cell Metab 2012, 16: 378–386.
48. Szczepanowska K, Trifunovic A. Tune instead of destroy: How proteolysis keeps OXPHOS in shape. Biochim Biophys Acta BBA Bioenerg 2021, 1862: 148365.
49. Li X, Chen C, Zhan X, Li B, Zhang Z, Li S, *et al*. R13 preserves motor performance in SOD1^{G93A} mice by improving mitochondrial function. Theranostics 2021, 11: 7294–7307.
50. Jiang X, Li L, Ying Z, Pan C, Huang S, Li L, *et al*. A small molecule that protects the integrity of the electron transfer chain blocks the mitochondrial apoptotic pathway. Mol Cell 2016, 63: 229–239.